Heterogeneous Tandem Catalysis Strategy for Additive-free CO_2 Hydrogenation into Formic Acid in Water: Crystal Plane Effect of Co_3O_4 Cocatalyst

Kohsuke Mori,[*ab] Jun Shinogi,[a] Yuki Shimada,[a] and Hiromi Yamashita[ab]

[a] Division of Materials and Manufacturing Science, Graduate School of Engineering, Osaka University, 2-1 Yamada-oka, Osaka 565-0871, Japan.

E-mail: mori@mat.eng.osaka-u.ac.jp

[b] Innovative Catalysis Science Division, Institute for Open and Transdisciplinary Research Initiatives (ICS-OTRI), Osaka University, Suita, Osaka 565-0871, Japan.

Abstract:

The transformation of carbon dioxide (CO_2) into formic acid (FA; HCOOH) in an aqueous phase is a promising method of realizing an environmentally friendly FA/CO_2-mediated chemical hydrogen storage/supply cycle. Despite progress in the design of catalysts that operate under basic conditions, the development of efficient catalysts that operate under additive-free conditions lags behind owing to the difficulty in activating CO_2 and the low solubility of CO_2 in pure water. In the present study, we present a heterogeneous tandem catalysis strategy in which Co_3O_4 is used as a CO_2 hydration cocatalyst to produce a HCO_3^- intermediate, in combination with our previously reported PdAg/TiO_2 as a catalyst for the hydrogenation of HCO_3^- to afford FA. The turnover number based on Pd improved by a factor of more than 8 in the presence of the Co_3O_4 cocatalyst with a cubic particle morphology enclosed by (100) facets. A series of morphology-controlled Co_3O_4 cocatalysts was investigated to elucidate the effect of the exposed crystal facets (i.e., (100), (111), or (112)) on their physicochemical properties and catalytic activity in FA synthesis. A systematic comparison based on experimental and density functional theory calculations demonstrated that the substantial enhancement effect of the Co_3O_4 cubes is attributable to the *in situ* generation of the largest amount of surface Co–OH groups with strong basicity originating from the exposed (100) facets. In addition, the present tandem catalytic system displayed high recyclability without exhibiting a structural change or a significant loss of activity. These findings will allow the rational design of an environmentally benign catalytic system for the hydrogenation of CO_2 to FA.

Keywords

Formic acid, Carbon dioxide, Tandem catalysis, Hydrogenation, Cobalt oxide

Introduction

The social demand for sustainable clean energy as well as CO_2 elimination has increased considerably in response to rapid climate change due to the increase of the CO_2 concentration in the atmosphere as a result of excessive combustion of fossil fuels.[1-3] The utilization of CO_2 as a renewable carbon source has aroused widespread interest.[4] The hydrogenation of CO_2 to formic acid (FA: HCOOH) is one promising approach to meet societal demands with remarkable versatility for utilization of emitted CO_2 as well as a promising strategy for efficient hydrogen storage. Interest in FA, in particular, stems from its high mass-based hydrogen content (52 g L^{-1}),

low toxicity, and nonflammability under ambient conditions.[5-10]

The synthesis of FA by the selective hydrogenation of CO_2 with H_2 involves a phase change from a gaseous reagent to a liquid product. Considering that the reactants are gases, the reaction is unfavorable in terms of the Gibbs free energy:[11]

$$H_2(g) + CO_2(g) \rightarrow HCOOH(l) \qquad \Delta G^0_{298} = 33.0 \text{ kJ mol}^{-1} \qquad \text{(eq. 1)}$$

Thus, this reaction is primarily conducted in an aqueous phase because of the relatively low corresponding Gibbs free energy change:[12]

$$H_2(aq) + CO_2(aq) \rightarrow HCOOH(l) \qquad \Delta G^0_{298} = -4 \text{ kJ mol}^{-1} \qquad \text{(eq. 2)}$$

To make the conversion of CO_2 to FA practically feasible, the thermodynamic equilibrium is shifted in the direction of the positive reaction through base reactions induced by adding organic amines or alkali/alkaline-earth bicarbonates, which interact with gaseous CO_2 to form bicarbonate in water:[13-20]

$$CO_2(aq) + H_2(aq) + B \rightarrow HCO_3^-(aq) + BH^+ \text{ (B: base)} \qquad \Delta G = -35.4 \text{ kJ mol}^{-1} \qquad \text{(eq. 3)}$$

We have previously demonstrated that PdAg nanoparticles (NPs) supported on TiO_2 exhibit an excellent turnover number (TON) in FA synthesis under aqueous basic conditions (**Figure 1a**).[21] High-angle annular dark-field scanning transmission electron microscopy (HAADF-STEM) observations as well as energy-dispersive X-ray spectroscopy (EDX) line analyses confirmed the formation of a highly dispersed random PdAg alloy (Pd/Ag = 30:70) with a mean particle diameter (d_{ave}) of 3.3 nm. X-ray absorption measurements indicate the presence of heteroatom Pd–Ag bonds (**Figure S1**). The alloying with Ag affects the electronic state of Pd, and we found that the enhanced electron-richness of the active Pd promotes the rate-determining reduction step for the adsorbed bicarbonate (HCO_3^-) by the dissociated hydride species, thereby enhancing the catalytic activity. Unfortunately, the use of bases is disfavored from the viewpoint of practical applications because the conversion of the resultant FA derivatives into pure FA is an exothermic process that requires acidification. Therefore, the development of an additive-free and environmentally friendly aqueous process based on eq. 2 would be beneficial.

Recently, several heterogeneous catalysts have been developed for this target reaction in the absence of additives.[13, 22-24] The main strategy is to use N-doped carbon materials as a support, resulting in a support that is hydrophilic and dispersible in pure water while exhibiting improved affinity toward CO_2. Our group has also reported that an N-doped polymer containing silica (NPS)

prepared by the reaction of 3-aminopropyltriethoxysilane with glutaraldehyde acts as a prominent support for PdAg NPs for the CO_2 hydrogenation into FA in water because of its high hydrophilicity and increased CO_2 adsorption capacity.[25] Despite this progress, the development of efficient catalysts that operate under additive-free conditions lags significantly behind that of catalysts that operate under basic conditions because of the difficulty in activating CO_2 and the low solubility of CO_2 in pure water. Therefore, alternative approaches that differ completely from the conventional catalyst design are strongly desired.

In the present study, we present a tandem catalytic process that combines Co_3O_4 as a CO_2 hydration cocatalyst with PdAg/TiO_2 as a hydrogenation catalyst to improve the catalytic activity under base-free conditions (**Figure 1b**). The Co_3O_4 enables the dissociation of water and the nucleophilic attack of OH^- on the dissolved CO_2 to form HCO_3^-. The PdAg/TiO_2 catalyst facilitates the dissociation of H_2 to afford a metal-hydride species, followed by adsorption of the HCO_3^- produced by the Co_3O_4 cocatalyst; the HCO_3^- then undergoes hydrogenation to give FA. The TON based on Pd was improved by a factor of more than 8 in the presence of cubic Co_3O_4. A facet engineering strategy is further used to clarify the effect of the morphology of the Co_3O_4 cocatalysts with cubic, octahedral, sheet, and plate structures on their physicochemical properties and catalytic activity in the FA synthesis. On the basis of a systematic comparison, we demonstrate that the substantial enhancement effect of cubic Co_3O_4 compared with the effects of the other Co_3O_4 structures is attributable the largest amount of surface Co–OH groups with strong basicity originating from the exposed (100) facet, as evidenced by experiments and density functional theory (DFT) calculations. The catalytic system described here is a promising candidate for a protocol for preparing FA under additive-free conditions because of its advantages of (i) a recyclable heterogeneous tandem catalyst, (ii) high catalytic activity and selectivity, and (iii) not requiring a homogeneous base.

Results and discussion

Morphological characterization of Co_3O_4

A fundamental insight into the correlation between the precisely controlled surface atomic arrangement of nanomaterials and their physicochemical properties is important for the rational design of heterogeneous catalysts with outstanding activity.[26-29] Spinel-structured Co_3O_4 is widely used in applications such as magnetism, optics, lithium-ion batteries, and heterogeneous catalysts.[30-32] Specifically, Co_3O_4 has two kinds of Co ions: Co^{2+} ions occupy one-eighth of the tetrahedral interstices, whereas Co^{3+} ions occupy one-half of the octahedral interstices.[33] The different crystal planes, such as (100), (111), and (112), display different atom arrangements;

therefore, the physicochemical properties of Co_3O_4 are closely associated with its morphology.[34-39]

Co_3O_4 cubes, octahedra, sheets, and plates were synthesized by a hydrothermal method under different conditions according to modified versions of previously reported procedures.[34, 40-41] For the Co_3O_4 particles, a commercially available specimen was used. The N_2 adsorption/desorption isotherms increased gradually without a substantial hysteresis loop (**Figure S2**). This type of isotherm can be classified as type III, reflecting the absence of micropores. The Brunauer–Emmett–Teller (BET) surface area increased in the order Co_3O_4 cubes (1.4 $m^2 g^{-1}$) < Co_3O_4 octahedra (2.5 $m^2 g^{-1}$) < Co_3O_4 plates (5.5 $m^2 g^{-1}$) < Co_3O_4 sheets (34.4 $m^2 g^{-1}$). The XRD patterns for all the samples show distinct peaks associated with face-centered cubic (FCC) Co_3O_4 (JCPDS 42-1467) (**Figure S3**). The crystal sizes were calculated using the Scherrer equation on the basis of the most prominent (311) diffraction peak, which increased in the order Co_3O_4 sheets (8.0 nm) < Co_3O_4 plates (8.8 nm) < Co_3O_4 octahedra (67.9 nm) < Co_3O_4 cubes (88.3 nm). The broadening of the reflections for Co_3O_4 sheets and Co_3O_4 plates is attributed to the low crystallinity of their thin layered structures.

The morphology and surface microstructures were investigated by transmission electron microscopy (TEM) and high-resolution TEM (HR-TEM) observations. The edge length of a Co_3O_4 cube is ~200 nm (**Figure 2a**). The (220) and (2−20) crystallographic planes of Co_3O_4 with a lattice spacing of 0.28 nm can be distinguished in the corresponding selected-area electron diffraction (SAED) pattern obtained along the [001] direction, implying that the Co_3O_4 cubes are only enclosed by (100) facets.[34] A TEM image of a Co_3O_4 octahedron shows that its edge length is ~250 nm and that the plane intersection angle is 70.5° (**Figure 2b**). Three sets of lattice fringes with spacings of 0.20, 0.28, and 0.46 nm are observed in the HR-TEM and SAED patterns, which we attribute to (002), (2−20), (1−1−1) planes, and/or their equivalent facets under the incident electron beam along the [110] direction.[37] These results confirm that the primary morphology is an octahedron enclosed by (111) facets. The Co_3O_4 sheet displays a hexagonal shape with a width of ~300 nm (**Figure 2c**). Two sets of lattice fringes with spacings of 0.23 and 0.28 nm are observed; they are attributed to (2−2−2) and (2−20) planes, respectively, along the [112] direction.[38] Thus, the dominant exposed facet of the Co_3O_4 sheet is (112). In the HR-TEM image of the Co_3O_4 plate, the spacing between lattice fringes with an angle of 60° is 0.28 nm (**Figure 2d**), corresponding to the (−202) and (0−22) planes.[42] These results confirm that the dominant exposed facet of the Co_3O_4 plate is (111).

The normalized Co K-edge X-ray absorption near edge structure (XANES) spectra for all Co_3O_4 specimens display similar edge absorption features (**Figure S4a**), where a pre-edge peak at 7705 eV corresponds to a sign of dipole forbidden 1s → 3d transition. All of the spectra also exhibit shoulder peaks at 7715 eV and a white line at 7722 eV because of a 1s → 4p transition.[43]

The Fourier transforms of the Co–K edge extended X-ray absorption fine structure (FT-EXAFS) spectra are displayed in **Figure S4b**. Three dominant peaks are observed at 1.56, 2.52, and 2.97 Å.[44-45] The first shorter peak can be assigned to two Co–O coordination shells including octahedral Co^{3+} and tetrahedral Co^{2+}, which were barely distinguishable because of their close proximity. The two longer peaks are ascribed to Co–Co coordination shells; the former is attributable to the distance between two octahedral Co ions (Co_{Oh}–Co_{Oh}), whereas the latter is likely related to the distance between two tetrahedral Co ions or tetrahedral and octahedral Co ions (Co_{Td}–Co_{Oh}/Co_{Td}). The absence of peak differences for all of the samples indicates that the morphology and the exposed face do not influence the local structures.

Hydrogenation of CO_2 into formic acid in water

The activities of a series of morphology-controlled Co_3O_4 cocatalysts were assessed during the hydrogenation of CO_2 into FA in the presence of a PdAg/TiO_2 catalyst. A typical reaction was performed in an autoclave under additive-free aqueous conditions with a total pressure of 2.0 MPa at 100 °C for 6 h using PdAg/TiO_2 as a catalyst (30 mg) and Co_3O_4 as a cocatalyst (30 mg). **Figure 3a** summarizes the TON values calculated on the basis of the total Pd loading amounts. The use of only the PdAg/TiO_2 catalyst without the Co_3O_4 cocatalyst resulted in a TON of 9.1. The addition of the Co_3O_4 cocatalyst substantially improved the activity by a factor of 3–9; interestingly, the enhancement effect was strongly influenced by the Co_3O_4 morphology. The TONs attained by the Co_3O_4 cocatalysts with cube, sheet, and plate morphologies were similar, whereas those attained with commercially available Co_3O_4 particles and Co_3O_4 with an octahedral morphology were relatively low. FA was obtained with 99% selectivity for all of the cocatalysts, and no byproducts were detected. The use of Co_3O_4/TiO_2 showed only low activity (TON =13), which further indicated the importance of the Co_3O_4 morphology. In the preliminary experiments, the PdAg/Co_3O_4 afforded a substantially lower TON of 9, implying that the Co_3O_4 did not serve as an effective support for the PdAg NPs. Notably, the reaction using only Co_3O_4 cocatalyst without PdAg/TiO_2 hardly proceeded. These results suggest that both PdAg/TiO_2 and Co_3O_4 are indispensable for attaining high activity.

As previously mentioned, the TONs attained by the Co_3O_4 cocatalysts with different morphologies, such as cube, sheet, and plate morphologies, were comparable, whereas the BET specific surface areas (S_{BET}) for these specimens differed substantially. To elucidate the effect of the exposed facets on the activity of the Co_3O_4 cocatalysts, the TONs were evaluated on the basis of the specific surface area of each Co_3O_4 cocatalyst (TON/S_{BET}). The results (**Figure 3b**) show that the Co_3O_4 cubes, which have six (100) planes preferentially exposed, exhibited superior activity compared with the Co_3O_4 octahedra, sheets, and plates, whose (111) or (112) planes are preferentially exposed. The obtained TON/S_{BET} ratios for the Co_3O_4 octahedra and plates are

comparable, which further confirms the ineffectiveness of (111) facets. Thus, the activity of the exposed Co_3O_4 planes follows the order (100) > (111) > (112).

The catalytic results obtained when other metal oxides and hydroxides were used as a cocatalyst instead of Co_3O_4 are shown in **Figure 3c**. CoO, ZrO_2, Nb_2O_5, and Ga_2O_3 gave poor results, and CeO_2 and $Co(OH)_2$ showed moderate activity for 24 h. The reaction using a layered double hydroxide (LDH) as a cocatalyst afforded a TON of 161; however, because of the LDH's strong basicity, ca. 70 wt% of it was dissolved by FA during the reaction at 100ºC under pressurized conditions.

The effect of temperature on the catalytic activity was also examined in experiments where Co_3O_4 was used as a cocatalyst (**Figure 3d**). The histogram of TON vs. temperature shows a volcano-type shape with a maximum activity at 100 °C. Interestingly, the addition of the Co_3O_4 cocatalyst provided relatively high activity even at 40 °C, whereas the reaction at 120 °C was substantially slower. An increase of the reaction temperature increases the favorability of the dehydrogenation of FA ($HCOOH \rightarrow H_2 + CO_2$) because the hydrogenation of CO_2 to FA is an exothermic reaction ($H_2 + CO_2 \rightarrow HCOOH$, $\Delta H_{298} = -31.2$ kJ mol^{-1}). This tendency is also explained by the trade-off relationship between the solubility of reaction gases (CO_2 and H_2) in water and the ability to overcome the activation energy; gases are well known to dissolve in water more readily at lower temperatures, thereby leading to increased activity. Indeed, increasing the total pressure improved the activity because of the higher solubility of CO_2 and H_2 and because of the shift of the equilibrium toward the direction with fewer molecules (**Figure 3e**). The maximum TON of 122 was attained at 4 MPa, whose TOF corresponds to 20 h^{-1}. This activity is comparable to or greater than those recently reported for other heterogeneous catalyst systems under additive-free conditions, including PdNi/carbon nanotubes (TOF = 0.2 h^{-1}, h^{-1}, 5 MPa),[13] Pd/g-C_3N_4 (TOF = 1.2 h^{-1}, 5 MPa),[24] 2Pd/ECN (TOF = 2.4 h^{-1},4 MPa),[23] PdAg/NPS(Glut) (TON = 200, TOF = 12.5 h^{-1}, 4 MPa),[25] Pd/Ac-SA (TOF = 29.1 h^{-1}, 4 MPa)[22], and PdMn0.6/AC-NH (TOF = 37.1 h^{-1}, 4 MPa).[46] Unfortunately, the attained catalytic activities are still low compared with those achieved in the presence of additives, such as $NaHCO_3$, NaOH, and NEt_3 (**Table S1**). Further studies are currently undergoing.

A more important advantage of the present catalytic system is the facile recovery of the catalyst from the reaction mixture and its high reusability. Upon completion of the hydrogenation reaction, the Co_3O_4 cubic cocatalyst could be recovered by filtration, along with the PdAg/TiO_2 catalyst. The combined powder sample could then be reused for CO_2 hydrogenation at least three times without loss of its inherent activity at 40 °C (**Figure 3f**). The XRD patterns (**Figure S5a**) show that the Co_3O_4 remained virtually unchanged, and no peaks attributable to Co metal or $CoCO_3$ were observed. TEM analysis also confirmed that the Co_3O_4 cubes maintained their morphology even after the reaction (**Figure S5b**). Co K-edge XAFS analysis further revealed no

changes in the oxidation state or local structure of the recovered Co_3O_4 (**Figure S5c and 5d**). Such characteristics might be due to the structural robustness of the Co_3O_4 cubes with exposed (100) planes, which is a pivotal contribution to the development of environmentally friendly chemical transformation processes. On the contrary, the TEM analysis of Co_3O_4 octahedra, Co_3O_4 plates, and Co_3O_4 sheets demonstrated that such Co_3O_4 specimen do not maintain their morphology after the reaction (**Figure S6**).

Mechanistic investigation

The process of catalytic hydration of CO_2 into H^+ and HCO_3^- at the adsorbed water–metal oxide interfaces has been previously well discussed. The hydration reaction of CO_2 with two H_2O molecules in pure aqueous solution has been previously calculated to be much more thermodynamically favorable than that with one H_2O molecule.[47] The important contribution of surface −OH groups on the metal oxides, such as Fe_2O_3 and γ-Al_2O_3, and adsorbed water molecules in the CO_2 hydration process was subsequently reported.[48-49] The theoretical calculations also confirmed that the activation energy in the reaction between CO_2 molecules and H_2O clusters coordinated to $Al(OH)_3$, which is an *M*−OH model, was lower than that for analogous clusters without $Al(OH)_3$.[50] More recently, Tyczkowski et al. demonstrated the critical role of –OH groups generated on the surface of plasma-deposited Co_3O_4-based thin films; the –OH groups are associated with strongly chemisorbed water molecules in the form of H_2O clusters.[51]

In an effort to understand the role of the Co_3O_4 cocatalyst in the CO_2 hydration process, the surface structure of Co_3O_4 was investigated by XPS during the hydrothermal (HT) treatment at 100 °C. The Co $2p_{3/2}$ spectra could be fitted to give three asymmetric peaks assigned to Co^{3+} at 779 eV, Co^{2+} at 781 eV, and a satellite peak at ~787 eV (**Figure S7**). Irrespective of the morphology, the Co^{3+}/Co^{2+} ratio for all of the Co_3O_4 cocatalysts before and after the HT treatment was almost constant at 2, suggesting that the oxidation states of the Co species did not substantially change. **Figure 4a–d** shows the O 1s spectra after the HT treatment for 6 h. The spectra could be deconvoluted into three peaks. The main peak at approximately 531 eV is assigned to Co–OH bonds (O_{OH}). The peak observed at 528 eV and the small peak at 533 eV are attributed to lattice oxygen (O_{latt}) and water molecules adsorbed onto the surface (O_{ad}).[38, 52] The O_{OH}/O_{latt} ratio for the Co_3O_4 cubes is 4.3, which is greater than the ratios of 3.2 and 3.0 for the octahedra/plates and sheets, respectively. **Figure 4e** shows the change in the O_{OH}/O_{latt} ratio as a function of the HT treatment time. The O_{OH}/O_{latt} ratio for all of the Co_3O_4 samples before the HT treatment was almost constant at 0.5; this ratio gradually increased with increasing time. The Co_3O_4 sheets exhibited a relatively high increment ratio at the initial stage; however, the slope

gradually decreased despite the large S_{BET} (34.4 $m^2\ g^{-1}$) of Co_3O_4 sheets. This result indicates that the (112) facets of the Co_3O_4 sheets easily reacted with H_2O, but the generated Co–OH bonds were not stable. However, the O_{OH}/O_{latt} ratios for the Co_3O_4 cubes and octahedra/plate increase linearly and show the highest values after 6 h of HT treatment. In particular, a more pronounced increase was observed for the Co_3O_4 cubes than for the octahedra/plate. This observation verifies the (100) facet over Co_3O_4 cube possess the easy reactivity with H_2O to produce Co−OH bond rather (111) facets and its reasonable stability under HT conditions rather than (112) facets. The details will be further discussed later.

The basic properties of each specimen before and after the HT treatment was evaluated via CO_2 temperature-programmed desorption (CO_2-TPD) experiments (**Figure 4f**). None of the CO_2-TPD spectra acquired before the HT treatment show distinguishable peaks, especially for Co_3O_4 cubes, indicating the absence of both Co–OH bonds and surface oxygen vacancies, which sometimes act as Lewis acid sites during CO_2 adsorption. After the Co_3O_4 cubes with exposed (100) planes were subjected to a HT treatment at 100 °C for 6 h, its CO_2-TPD spectrum displayed a distinct desorption peak centered at 475 °C. The spectra of the Co_3O_4 octahedra and plates, which have exposed (111) planes, also exhibited a moderate desorption peak in the range 350–500 °C, whereas a broad peak was observed from ~350 and ~450 °C for Co_3O_4 sheets, which have exposed (112) planes. **Figure 4g** shows a comparison of the total amount of adsorbed CO_2 based on the surface area of each cocatalyst ($mol_{CO2}\cdot m^{-2}{}_{Co3O4}$), which increased in the order sheets < octahedra/plates < cubes. This tendency agrees well with the catalytic activity based on surface area in the synthesis of FA under additive-free conditions (**Figure 3b**). The HT-treated Co_3O_4 cubes possess much more basic sites with relatively stronger basicity as a result of their higher concentration of Co–OH bonds; they also exhibit enhanced CO_2 hydration activity.

Based on the previous experimental investigations as well as theoretical calculation studies regarding the reaction mechanisms, we propose a possible catalytic cycle for CO_2 hydration over Co_3O_4 (**Figure 5a**) (**Path 1**).[53-56] The reaction is initiated by the adsorption of H_2O (***step 1***). The dissociation of H_2O then occurs to afford a Co–OH species (***step 2***), followed by the adsorption of CO_2 (***step 3***). The adsorbed CO_2 undergoes hydration to give a HCO_3^- intermediate based on the attack of active Co–OH on the C atoms of the adsorbed CO_2 (***step 4***). On the other hand, the dissociation of H_2 occurs over PdAg/TiO_2 to afford a metal hydride species. The HCO_3^- generated in situ on Co_3O_4 subsequently undergoes the attack of an active hydride species on the C atom of the HCO_3^- to produce a formate intermediate. Finally, the attack of another H atom on the O atom of the OH group produces formate and H_2O, regenerating the initial active metal species.

To better understand the effect of the crystal planes of the Co_3O_4 cocatalyst, the corresponding potential energy profiles were obtained using DFT calculations in which Co_3O_4 (100), Co_3O_4 (111), and Co_3O_4 (112) slabs were used as models for cubes, octahedra/plates, and sheets,

respectively (**Figure 5b and c**). In the case of Co_3O_4(100), the adsorption energy of H_2O is 1.56 eV (*step 1*). No substantial differences are observed in the adsorption energies of H_2O for Co_3O_4(111) and Co_3O_4(112). The dissociation of H_2O occurs at vicinal Co–O–Co sites via $TS_{II/III}$ with a barrier of 1.02 eV over Co_3O_4(100) (*step 2*). This activation energy is slightly higher than the value of 0.83 eV calculated for Co_3O_4(112) but is substantially lower than that of 2.18 eV determined for Co_3O_4(111). These results agree with the initial O_{OH}/O_{latt} ratio obtained from the O 1s XPS analysis after HT treatment, where the O_{OH}/O_{latt} formation rate increased in the order octahedra/plate < cubes < sheets.

We subsequently determined the adsorption energy for CO_2 to be 0.27 eV for Co_3O_4(100) (*step 3*), which is consistent with those obtained for Co_3O_4(111) and Co_3O_4(112). Finally, the hydration of the adsorbed CO_2 occurs through the attack of a Co–OH species via $TS_{IV/V}$, with a barrier of 0.23 eV for Co_3O_4(100) (*step 4*). This activation energy is slightly lower than the value of 0.37 eV obtained for Co_3O_4(111) but is substantially lower than the 1.27 eV calculated for Co_3O_4(112). These calculation results are consistent with the amount of basic sites determined by CO_2 adsorption (**Figure 4g**), where the amount of basic sites based on each surface area ($mol_{CO2}\cdot m^{-2}{}_{Co3O4}$) was found to increase in the order sheets < octahedra/plates < cubes. The obtained energy diagram demonstrates that the rate-determining step is dependent on the crystal plane of Co_3O_4; for Co_3O_4(100) and (111), the H_2O dissociation is the rate-determining step, whereas the hydration of CO_2 is the rate-determining step for Co_3O_4(112). Notably, Co_3O_4(100) does not require the large-energy-input overall reaction despite the presence of a rate-determining step. This result explains the high activity of the Co_3O_4 cubes with (100) facets. In a preliminary calculation, we investigated the potential energy profile in Path 2 for Co_3O_4 (100), where the adsorption of CO_2 occurs prior to the adsorption of H_2O. The activation energies for the dissociation of H_2O and the hydration of CO_2 were determined to be 1.20 and 1.21 eV, respectively. Thus, the hydration of CO_2 is energetically more likely to proceed if H_2O is primarily adsorbed rather than CO_2.[57]

As previously discussed, the reactivity of each Co_3O_4 facet with H_2O to produce Co–OH bonds (*step 1*) follows the order (112) > (100) > (111). This result is presumably explained by the total number density of dangling bonds of Co^{3+} and Co^{2+} ions on the corresponding facets, which follows the order (112) (24.99 nm^{-2}) > (100) (18.36 nm^{-2}) > (111) (17.67 nm^{-2}).[39] A catalytic reaction including bond breaking is generally promoted by a distorted crystal structure with enhanced electron density. The high number density of dangling bonds on the Co_3O_4(112) surfaces implies that they have unique surface electronic structures that are responsible for the high reactivity. Moreover, the topmost layer of the (112) facet of the Co_3O_4 is more open than the other low-index (100) and (111) surfaces, which allows H_2O molecules to easily access the sublayer Co^{3+} cations.[34] On the contrary, the relatively smaller (100) surface energy of (100) (0.92 J m^{-2})

compared with that of for (112) (1.46 J m^{-2}) might account for the greater stability of the formed Co–OH bond over the (100) face under HT conditions compared with that of the formed Co–OH bond over the (112) face,[37] which was determined by monitoring the O_{OH}/O_{latt} ratios obtained from O 1s XPS spectra acquired during the HT treatment at 100 °C (**Figure 4e**).

The enhancement of the hydration of the CO_2 (*step 4*) adsorbed onto the (100) and (111) surfaces compared with that of CO_2 adsorbed onto the (112) surface can be explained not only by the difference in the amounts of basic sites (**Figure 3f**) but also by the basicity of the Co–OH species. The Co–OH bond distance determined from the DFT-optimized geometries follows the order (100) (1.919 Å) > (111) (1.820 Å) > (112) (1.806 Å), as shown in **Figure S8**. The basicity of metal oxides tends to correlate with the length of *M*–O bonds because the Coulomb force between two atoms is weak and the mobility of oxygen atoms is increased.[58] Therefore, a longer bond will produce a weaker Coulomb force between atoms; oxygen mobility is thereby increased on the (100) facet compared with that on the (111) and (112) facets. These results are indicative of a higher concentration of Co–OH bonds with increasing basicity over the (100) surfaces compared with the corresponding concentration over the and (111) and (112) surface.

Furthermore, the d-band center theory was exploited to confirm the basicity of Co–OH bonds. Generally, the difference in adsorption capacity is mainly due to the antibonding state. In other words, a lower d-band center compared to the Fermi level of the active metal indicates a downward shift in the antibonding state, which results in weaker bonding with a longer M–O bond. Density of states (DOS) calculations showed that the d-band center of Co atoms within Co_3O_4 located at -0.685 eV, -0.631 eV, and -0.614 eV for (100), (111), and (112), respectively (**Figure 6)**. It is therefore concluded that the antibonding state of the Co atoms of (100) is deeper than those of (111) and (112), which results in a weaker interaction between the Co atoms of (100) and OH, and finally affording a higher basicity.

Conclusion

In this study, a heterogeneous tandem catalysis strategy was first proposed to achieve additive-free hydrogenation of CO_2 into FA in water using Co_3O_4 as a CO_2 hydration cocatalyst in conjunction with $PdAg/TiO_2$ as a hydrogenation catalyst to afford FA. The effect of the surface facets of the Co_3O_4 nanocrystals on their physicochemical properties and activity as a cocatalyst was elucidated using a series of morphologically tailored specimens enclosed by different crystal planes, such as cubes, octahedra, sheets, and plates. The Co_3O_4 cubes, which were enclosed by (100) facets, exhibited enhanced activity compared with the other Co_3O_4 cocatalysts with exposed (111) and (112) facets. Moreover, the Co_3O_4 cubes were highly robust and durable. No substantial degradation was observed, and the exposed surface facet was retained. XPS analysis, CO_2-TPD

measurements, and DFT calculations revealed that Co_3O_4(100) does not require a large-energy-input overall reaction sequence because it possesses many more basic sites with relatively stronger basicity as a result of its higher concentration of Co–OH bonds. This study offers not only a promising durable heterogeneous tandem catalytic system with potential practical applications but also demonstrates the importance of precisely tuning the exposed surface crystal facets of the catalyst.

Experimental Section

Materials: All chemicals were used as received without purification. $Pd(NH_3)_4Cl_2$ was obtained from Sigma-Aldrich. Co_3O_4 particle was obtained from Wako. $Co(NO_3)_2{\cdot}6H_2O$ and $AgNO_3$ were purchased from Nacalai Tesque.

Synthesis of Co_3O_4 cubes:[40] $Co(NO_3)_2{\cdot}6H_2O$ (3.5 g) and NaOH (0.12 g) were added to distilled water (12 mL) under magnetic stirring for 30 min. The resultant solution was transferred into an autoclave with a Teflon liner and heated at 180 °C for 12 h, followed by cooling, separation, washing with ethanol and water, and drying under vacuum. The obtained material was calcined in air at 500 °C for 3 h.

Synthesis of Co_3O_4 sheets:[33] $Co(NO_3)_2{\cdot}6H_2O$ (1 mmol, 0.291 g) in distilled water (20 mL) was added to a solution of oleylamine (4 mL) and EtOH (10 mL), and the resultant mixture was stirred for 30 min using a magnetic stirrer. The solution was then transferred into an autoclave with a Teflon liner and heated at 180 °C for 12 h, followed by cooling, separation, washing with ethanol and water, and drying under vacuum. The obtained powder was calcined in air at 350 °C for 3 h.

Synthesis of Co_3O_4 octahedra:[40] $Co(NO_3)_2{\cdot}6H_2O$ (17.5 g) and NaOH (0.8 g) were added to distilled water (12 mL), and the resultant mixture was stirred for 30 min using a magnetic stirrer. The solution was then transferred to an autoclave with a Teflon liner and heated at 200 °C for 12 h, followed by cooling, separation, washing with ethanol and water, and drying under vacuum. The obtained powder was calcined in air at 500 °C for 3 h.

Synthesis of Co_3O_4 plates:[42] $Co(OAc)_2$ (250 mg) in ethylene glycol (18 mL) solution was transferred into an autoclave with a Teflon liner and heated at 200 °C for 18 h, followed by cooling, separation, washing with ethanol and water, and drying under vacuum. The obtained powder was calcined in air at 350 °C for 3 h.

Catalyst synthesis: TiO_2 (0.5 g, supplied from Catalysis Society of Japan), $Pd(NH_3)_4Cl_2$ (0.047 mmol), and $AgNO_3$ (0.047 mmol) were added to 100 mL of an aqueous solution and the resultant mixture was stirred at room temperature. After 1h, the solvent was removed using a rotary evaporator, and the resultant powder was dried overnight. The sample was subsequently reduced with $NaBH_4$ (0.28 mmol) to give $PdAg/TiO_2$ (Pd: 1.0 wt%, Pd/Ag molar ratio = 1/1).

Characterization: Powder XRD patterns, N_2 adsorption–desorption measurement, inductively coupled plasma atomic emission spectroscopy analysis, XPS, and CO_2-TPD experiments were acquired according to procedures described previously.[29] High-resolution TEM images and SAED patterns were obtained with a JEOL ARM200F instrument operating at 200 kV. Co K-edge XAFS spectra were recorded at the 01B1 beamline station at the SPring-8 facility, JASRI, Harima, Japan (2023A1668 and 2023B1805) by transmission mode with a Si(111) monochromator. Data reduction was performed using the REX2000 software program (Rigaku).

DFT calculations: The CASTEP program in the Materials Studio 17.2 software package was used to perform the DFT calaculations.[41, 59] The GGA exchange–correlation functional proposed by PBE was combined with the DNP. The periodic boundary conditions were applied to the Co_3O_4 slabs consisting of a 3 × 3 (100) supercell with cell dimensions of 11.4353 × 11.4353 × 24.1358 $Å^3$, a 3 × 3 (111) supercell with a cell dimensions of 11.4353 × 11.4353 ×24.0849 $Å^3$, and a 3 × 3 (112) supercell with cell dimensions of 5.7177 × 14.0054 × 24.0359 $Å^3$, respectively. All surface slabs constructed were augmented with 20 Å of vacuum in the z-direction. The reactant atoms and the top Co3O4 layer were relaxed during geometry optimizations, and other layers were fixed at the corresponding bulk positions. In the calculation of the DOS for a series of Co_3O_4, the Hubbard U correction (DFT+U) was adopted to properly describe the correlation energy of the strongly localized 3d orbital of the Co metals (U=4.0 eV).[60]

General procedure for additive-free CO_2 hydrogenation: The catalytic activity was assessed using a stainless steel autoclave (60 mL). In a typical trial, the PdAg/TiO_2 catalyst (30 mg), Co_3O_4 cocatalyst (30 mg), and distilled water (15 mL) were added to the reactor. The autoclave was sealed and flushed with CO_2. The reaction was pressurized first with CO_2 to 1.0 MPa and then with H_2 to 2.0 MPa. The system was subsequently heated to 100 °C and stirred for 6 h. After cooling to room temperature, the pressure in the reactor was gradually released. FA yields were determined with HPLC using a Shimadzu instrument equipped with a Bio-Rad Aminex HPX-87H ion-exclusion column (300 × 7.8 mm^2) with 5 mM H_2SO_4 (5 mM, 0.5 mL min^{-1}) as the mobile phase at 40 °C. TON values were determined by according to the following equation; TON = [mol of FA produced after 6h]/[total mole of Pd].

After the reaction, the mixture of powdered catalyst and cocatalyst was recovered by centrifugation, washed twice with water and ethanol, then redispersed in water and used for repeated tests under the same conditions described above.

Corresponding Author

Kohsuke Mori

Division of Materials and Manufacturing Science, Graduate School of Engineering, Osaka University, 2-1 Yamada-oka, Osaka 565-0871, Japan

Anisotropic Design & Additive Manufacturing Research Center, Osaka University, 2-1, Yamadaoka, Suita, Osaka 565-0871, Japan

Innovative Catalysis Science Division, Institute for Open and Transdisciplinary Research Initiatives (OTRI), Osaka University, 2-1 Yamadaoka, Suita, Osaka 565-0871, Japan

ORCID http://orcid.org/0000-0003-3915-4528

E-mail: mori@mat.eng.osaka-u.ac.jp

Authors

Jun Shinogi

Division of Materials and Manufacturing Science, Graduate School of Engineering, Osaka University, 2-1 Yamada-oka, Osaka 565-0871, Japan

Yuki Shimada

Division of Materials and Manufacturing Science, Graduate School of Engineering, Osaka University, 2-1 Yamada-oka, Osaka 565-0871, Japan

Hiromi Yamashita

Division of Materials and Manufacturing Science, Graduate School of Engineering, Osaka University, 2-1 Yamada-oka, Osaka 565-0871, Japan

Innovative Catalysis Science Division, Institute for Open and Transdisciplinary Research Initiatives (OTRI), Osaka University, 2-1 Yamadaoka, Suita, Osaka 565-0871, Japan

ORCID http://orcid.org/0000-0003-1796-5776

Author contributions

K.M. supervised the project and wrote the manuscript. J.S. performed the catalyst preparation, characterization, and catalytic reactions. Y.S. helped catalytic reactions. H.Y. helped supervise the project.

Declaration of competing interest

There are no conflicts to declare.

Supporting Information

Supporting Information is available free of charge via the Internet at http://pubs.acs.org, XAFS, N_2 adsorption–desorption isotherm, XRD, TEM, XPS.

Acknowledgements

This work was financially supported by Grants-in-Aid for Scientific Research (A21H050980 and T22K189200) from the Japan Society for the Promotion of Science (JSPS). Part of this work was supported by Yazaki Memorial Foundation for Science and Technology. Part of TEM experiment was carried out by using a facility in the Research Center for Ultra-High Voltage Electron Microscopy, Osaka University.

References

1. Jessop, P. G.; Ikariya, T.; Noyori, R., Homogeneous Hydrogenation of Carbon Dioxide. *Chem. Rev.* **1995,** *95* (2), 259-272.

2. Wang, W.; Wang, S.; Ma, X.; Gong, J., Recent Advances in Catalytic Hydrogenation of Carbon Dioxide. *Chem. Soc. Rev.* **2011,** *40* (7), 3703-3727.

3. Kondratenko, E. V.; Mul, G.; Baltrusaitis, J.; Larrazabal, G. O.; Perez-Ramirez, J., Status and Perspectives of CO_2 Conversion into Fuels and Chemicals by Catalytic, Photocatalytic and Electrocatalytic Processes. *Energy Environ. Sci.* **2013,** *6* (11), 3112-3135.

4. Álvarez, A.; Bansode, A.; Urakawa, A.; Bavykina, A. V.; Wezendonk, T. A.; Makkee, M.; Gascon, J.; Kapteijn, F., Challenges in the Greener Production of Formates/Formic Acid, Methanol, and DME by Heterogeneously Catalyzed CO2 Hydrogenation Processes. *Chem. Rev.* **2017,** *117* (14), 9804-9838.

5. Eppinger, J.; Huang, K.-W., Formic Acid As A Hydrogen Energy Carrier. *ACS Energy Lett.* **2017,** *2* (1), 188-195.

6. Grasemann, M.; Laurenczy, G., Formic Acid as a Hydrogen Source - Recent Developments and Future Trends. *Energy Environ. Sci.* **2012,** *5* (8), 8171-8181.

7. Mellmann, D.; Sponholz, P.; Junge, H.; Beller, M., Formic Acid as a Hydrogen Storage Material - Development of Homogeneous Catalysts for Selective Hydrogen Release. *Chem. Soc. Rev.* **2016,** *45* (14), 3954-3988.

8. Verma, P.; Zhang, S.; Song, S.; Mori, K.; Kuwahara, Y.; Wen, M.; Yamashita, H.; An, T., Recent

Strategies for Enhancing the Catalytic Activity of CO_2 Hydrogenation to Formate/Formic Acid over Pd-based Catalyst. *J. CO_2 Util.* **2021,** *54*, 101765.

9. Joó, F., Breakthroughs in Hydrogen Storage—Formic Acid as a Sustainable Storage Material for Hydrogen. *ChemSusChem* **2008,** *1* (10), 805-808.

10. Wang, W.-H.; Hull, J. F.; Muckerman, J. T.; Fujita, E.; Himeda, Y., Second-coordination-sphere and Electronic Effects Enhance Iridium(Iii)-Catalyzed Homogeneous Hydrogenation of Carbon Dioxide in Water Near Ambient Temperature and Pressure. *Energy Environ. Sci.* **2012,** *5* (7), 7923-7926.

11. Moret, S.; Dyson, P. J.; Laurenczy, G., Direct Synthesis of Formic Acid from Carbon Dioxide by Hydrogenation in Acidic Media. *Nat. Commun.* **2014,** *5*, 4017.

12. Jessop, P. G.; Joó, F.; Tai, C.-C., Recent Advances in the Homogeneous Hydrogenation of Carbon Dioxide. *Coord. Chem. Rev.* **2004,** *248* (21), 2425-2442.

13. Nguyen, L. T. M.; Park, H.; Banu, M.; Kim, J. Y.; Youn, D. H.; Magesh, G.; Kim, W. Y.; Lee, J. S., Catalytic CO_2 Hydrogenation to Formic Acid over Carbon Nanotube-Graphene Supported PdNi Alloy Catalysts. *RSC Adv.* **2015,** *5* (128), 105560-105566.

14. Masuda, S.; Mori, K.; Futamura, Y.; Yamashita, H., PdAg Nanoparticles Supported on Functionalized Mesoporous Carbon: Promotional Effect of Surface Amine Groups in Reversible Hydrogen Delivery/Storage Mediated by Formic Acid/CO_2. *ACS Catal.* **2018,** *8* (3), 2277-2285.

15. Masuda, S.; Mori, K.; Kuwahara, Y.; Yamashita, H., PdAg Nanoparticles Supported on Resorcinol-Formaldehyde Polymers Containing Amine Groups: the Promotional Effect of Phenylamine Moieties on CO_2 Transformation to Formic Acid. *J. Mater. Chem. A* **2019,** *7* (27), 16356-16363.

16. Mori, K.; Hata, H.; Yamashita, H., Interplay of Pd ensemble sites induced by GaO_x modification in boosting CO_2 hydrogenation to formic acid. *Appl. Catal. B: Environ.* **2023,** *320*, 122022.

17. Mori, K.; Konishi, A.; Yamashita, H., Interfacial Engineering of PdAg/TiO_2 with a Metal–Organic Framework to Promote the Hydrogenation of CO_2 to Formic Acid. *J. Phys. Chem. C* **2020,** *124* (21), 11499-11505.

18. Mori, K.; Masuda, S.; Tanaka, H.; Yoshizawa, K.; Che, M.; Yamashita, H., Phenylamine-functionalized Mesoporous Silica Supported PdAg Nanoparticles: a Dual Heterogeneous Catalyst for Formic Acid/CO_2-mediated Chemical Hydrogen Delivery/Storage. *Chem. Commun.* **2017,** *53*, 4677-4680.

19. Mori, K.; Taga, T.; Yamashita, H., Isolated Single-Atomic Ru Catalyst Bound on a Layered Double Hydroxide For Hydrogenation of CO_2 to Formic Acid. *ACS Catal.* **2017,** *7* (5), 3147-3151.

20. Gunasekar, G. H.; Park, K.; Jung, K.-D.; Yoon, S., Recent Developments in the Catalytic Hydrogenation of CO_2 to Formic Acid/Formate using Heterogeneous Catalysts. *Inorg. Chem. Front.* **2016,** *3* (7), 882-895.

21. Mori, K.; Sano, T.; Kobayashi, H.; Yamashita, H., Surface Engineering of a Supported PdAg Catalyst for Hydrogenation of CO_2 to Formic Acid: Elucidating the Active Pd Atoms in Alloy Nanoparticles. *J. Am. Chem. Soc.* **2018,** *140* (28), 8902-8909.

22. Jiang, S.; Liu, X.; Zhai, S.; Ci, X.; Yu, T.; Sun, L.; Zhai, D.; Deng, W.; Ren, G., Additive-free CO_2 Hydrogenation to Pure Formic Acid Solution via Amine-modified Pd Catalyst At Room Temperature. *Green Chem.* **2023,** *25* (15), 6025-6031.

23. Mondelli, C.; Puértolas, B.; Ackermann, M.; Chen, Z.; Pérez-Ramírez, J., Enhanced Base-Free Formic Acid Production from CO_2 on Pd/g-C_3N_4 by Tuning of the Carrier Defects. *ChemSusChem* **2018,** *11* (17), 2859-2869.

24. Park, H.; Lee, J. H.; Kim, E. H.; Kim, K. Y.; Choi, Y. H.; Youn, D. H.; Lee, J. S., A highly Active and Stable Palladium Catalyst on a g-C_3N_4 Support for Direct Formic Acid Synthesis under Neutral Conditions. *Chem. Commun.* **2016,** *52* (99), 14302-14305.

25. Masuda, S.; Mori, K.; Kuwahara, Y.; Louis, C.; Yamashita, H., Additive-Free Aqueous Phase Synthesis of Formic Acid by Direct CO_2 Hydrogenation over a PdAg Catalyst on a Hydrophilic N-Doped Polymer–Silica Composite Support with High CO_2 Affinity. *ACS Appl. Energy Mater.* **2020,** *3* (6), 5847-5855.

26. Xia, Y.; Xiong, Y.; Lim, B.; Skrabalak, S. E., Shape-Controlled Synthesis of Metal Nanocrystals: Simple Chemistry Meets Complex Physics? *Angew. Chem. Inter. Ed.* **2009,** *48* (1), 60-103.

27. Zhou, K.; Li, Y., Catalysis Based on Nanocrystals with Well-Defined Facets. *Angew. Chem. Inter. Ed.* **2012,** *51* (3), 602-613.

28. Mori, K.; Jida, H.; Kuwahara, Y.; Yamashita, H., CoOx-decorated CeO_2 Heterostructures: Effects of Morphology on Their Catalytic Properties in Diesel Soot Combustion. *Nanoscale* **2020,** *12* (3), 1779-1789.

29. Hashimoto, N.; Mori, K.; Matsuzaki, S.; Iwama, K.; Kitaura, R.; Kamiuchi, N.; Yoshida, H.; Yamashita, H., Sub-nanometric High-Entropy Alloy Cluster: Hydrogen Spillover Driven Synthesis on CeO_2 and Structural Reversibility. *JACS Au* **2023,** *3* (8), 2131-2143.

30. Ding, J.; Hu, W.; Paek, E.; Mitlin, D., Review of Hybrid Ion Capacitors: From Aqueous to Lithium to Sodium. *Chem. Rev.* **2018,** *118* (14), 6457-6498.

31. He, Q.; Wang, H.; Zhao, X.; Chen, L., Recent advances of transition metal oxalate-based micro- and nanomaterials for electrochemical energy storage: a review. *Mater. Today Chem.* **2021,** *22*, 100564.

32. Jiao, F.; Frei, H., Nanostructured Cobalt and Manganese Oxide Clusters as Efficient Water Oxidation Catalysts. *Energy Environ. Sci.* **2010,** *3* (8), 1018-1027.

33. Xie, X.; Shen, W., Morphology Control of Cobalt Oxidenanocrystals for Promoting their Catalytic Performance. *Nanoscale* **2009,** *1* (1), 50-60.

34. Hu, L.; Peng, Q.; Li, Y., Selective Synthesis of Co3O4 Nanocrystal with Different Shape and Crystal Plane Effect on Catalytic Property for Methane Combustion. *J. Am. Chem. Soc.* **2008,** *130* (48), 16136-16137.

35. Mu, J.; Zhang, L.; Zhao, G.; Wang, Y., The Crystal Plane Effect on the Peroxidase-Like Catalytic Properties of Co_3O_4 Nanomaterials. *Phys.Chem.Chem.Phys* **2014,** *16* (29), 15709-15716.

36. Yao, J.; Shi, H.; Sun, D.; Lu, H.; Hou, B.; Jia, L.; Xiao, Y.; Li, D., Facet-Dependent Activity of Co_3O_4 Catalyst for C_3H_8 Combustion. *ChemCatChem* **2019,** *11* (22), 5570-5579.

37. Su, D.; Dou, S.; Wang, G., Single Crystalline Co_3O_4 Nanocrystals Exposed with Different Crystal Planes for Li-O_2 Batteries. *Sci. Rep.* **2014,** *4* (1), 5767.

38. Zhou, X.; Liu, Z.; Wang, Y.; Ding, Y., Facet Effect of Co_3O_4 Nanocrystals on Visible-Light Driven Water Oxidation. *Appl. Catal. B: Environ.* **2018,** *237*, 74-84.

39. Cai, Y.; Xu, J.; Guo, Y.; Liu, J., Ultrathin, Polycrystalline, Two-Dimensional Co_3O_4 for Low-Temperature CO Oxidation. *ACS Catal.* **2019,** *9* (3), 2558-2567.

40. Xiao, X.; Liu, X.; Zhao, H.; Chen, D.; Liu, F.; Xiang, J.; Hu, Z.; Li, Y., Facile Shape Control of Co_3O_4 and the Effect of the Crystal Plane on Electrochemical Performance. *Adv. Mater.* **2012,** *24* (42), 5762-5766.

41. Payne, M. C.; Teter, M. P.; Allan, D. C.; Arias, T. A.; Joannopoulos, J. D., Iterative Minimization Techniques for ab Initio Total-Energy Calculations: Molecular Dynamics and Conjugate Gradients. *Rev. Mod. Phys.* **1992,** *64* (4), 1045-1097.

42. Yu, X.-Y.; Meng, Q.-Q.; Luo, T.; Jia, Y.; Sun, B.; Li, Q.-X.; Liu, J.-H.; Huang, X.-J., Facet-dependent Electrochemical Properties of Co_3O_4 Nanocrystals toward Heavy Metal Ions. *Sci. Rep.* **2013,** *3* (1), 2886.

43. Sa, Y. J.; Kwon, K.; Cheon, J. Y.; Kleitz, F.; Joo, S. H., Ordered Mesoporous Co_3O_4 Spinels as Stable, Bifunctional, Noble Metal-free Oxygen Electrocatalysts. *J. Mater. Chem. A* **2013,** *1* (34), 9992-10001.

44. Huffman, G. P.; Shah, N.; Zhao, J. M.; Huggins, F. E.; Hoost, T. E.; Halvorsen, S.; Goodwin, J. G., In-Situ XAFS Investigation of K-Promoted Co Catalysts. *J. Catal.* **1995,** *151* (1), 17-25.

45. Moen, A.; Nicholson, D. G.; Clausen, B. S.; Hansen, P. L.; Molenbroek, A.; Steffensen, G., X-ray Absorption Spectroscopic Studies at the Cobalt K-Edge on a Reduced Al_2O_3-Supported Rhenium-Promoted Cobalt Fischer−Tropsch Catalyst. *Chem. Mater.* **1997,** *9* (5), 1241-1247.

46. Ci, X.; Zhai, D.; Tu, R.; Li, X.; Jiang, S.; Wang, X.; Deng, W.; Ren, G., Continuous Production of Pure Formic Acid Solution from CO_2 Hydrogenation at Room Temperature via Amine-Functionalized Pdmn Nano-Alloy. *Chem. Eng. J.* **2024,** *497*, 154951.

47. Merz, K. M., Jr., Gas-phase and Solution-Phase Potential Energy Surfaces for Carbon Dioxide + n-water (n = 1,2). *J. Am. Chem. Soc.* **1990,** *112* (22), 7973-7980.

48. Baltrusaitis, J.; Grassian, V. H., Surface Reactions of Carbon Dioxide at the Adsorbed Water−Iron Oxide Interface. *J. Phys. Chem. B* **2005,** *109* (25), 12227-12230.

49. Baltrusaitis, J.; Schuttlefield, J. D.; Zeitler, E.; Jensen, J. H.; Grassian, V. H., Surface Reactions of Carbon Dioxide at the Adsorbed Water−Oxide Interface. *J. Phys. Chem. C* **2007,** *111* (40), 14870-14880.

50. Baltrusaitis, J.; Grassian, V. H., Carbonic Acid Formation from Reaction of Carbon Dioxide and Water Coordinated to Al(OH)3: A Quantum Chemical Study. *J. Phys. Chem. A* **2010,** *114* (6), 2350-2356.

51. Kierzkowska-Pawlak, H.; Kruszczak, E.; Tyczkowski, J., Catalytic Activity of Plasma-Deposited Co_3O_4-Based Thin Films for CO_2 Hydration – A New Approach to Carbon Capture Applications. *Appl. Catal. B: Environ.* **2022,** *304*, 120961.

52. Menezes, P. W.; Indra, A.; González-Flores, D.; Sahraie, N. R.; Zaharieva, I.; Schwarze, M.; Strasser, P.; Dau, H.; Driess, M., High-Performance Oxygen Redox Catalysis with Multifunctional Cobalt Oxide Nanochains: Morphology-Dependent Activity. *ACS Catal.* **2015,** *5* (4), 2017-2027.

53. Filonenko, G. A.; Vrijburg, W. L.; Hensen, E. J. M.; Pidko, E. A., On the Activity of Supported Au Catalysts in the Liquid Phase Hydrogenation of CO_2 to Formates. *J. Catal.* **2016,** *343*, 97-105.

54. Wiener, H.; Blum, J.; Feilchenfeld, H.; Sasson, Y.; Zalmanov, N., The Heterogeneous Catalytic Hydrogenation of Bicarbonate to Formate in Aqueous Solutions. *J. Catal.* **1988,** *110* (1), 184-190.

55. He, C.-S.; Gong, L.; Zhang, J.; He, P.-P.; Mu, Y., Highly Selective Hydrogenation of CO_2 into Formic Acid on a Nano-Ni Catalyst at Ambient Temperature: Process, Mechanisms and Catalyst Stability. *J. CO_2 Util.* **2017,** *19*, 157-164.

56. Oh, K.-R.; Han, Y.; Cha, G.-Y.; Valekar, A. H.; Lee, M.; Sivan, S. E.; Kwon, Y.-U.; Hwang, Y. K., Carbonic Anhydrase-Mimicking Keplerate Cluster Encapsulated Iron Trimesate for Base-Free CO_2 Hydrogenation. *ACS Sustainable Chem. Eng.* **2021,** *9* (42), 14051-14060.

57. Raksakoon, C.; Maihom, T.; Probst, M.; Limtrakul, J., Hydration of Carbon Dioxide in Copper-Alkoxide Functionalized Metal–Organic Frameworks: A DFT Study. *J. Phys. Chem. C* **2015,** *119* (7), 3564-3571.

58. Mori, K.; Shimoji, Y.; Yamashita, H., Improved Low-Temperature Hydrogen Production from Aqueous Methanol Based on Synergism between Cationic Pt and Interfacial Basic LaO_x. *ChemSusChem* **2023,** *16* (16), e202300283.

59. Milman, V.; Winkler, B.; White, J. A.; Pickard, C. J.; Payne, M. C.; Akhmatskaya, E. V.; Nobes, R. H., Electronic Structure, Properties, and Phase Stability of Inorganic Crystals: A Pseudopotential Plane-Wave Study. *Inter. J. Quantum Chem.* **2000,** *77* (5), 895-910.

60. Dudarev, S. L.; Botton, G. A.; Savrasov, S. Y.; Humphreys, C. J.; Sutton, A. P., Electron-energy-loss Spectra and the Structural Stability of Nickel Oxide: An LSDA+U Study. *Phys. Rev. B* **1998,** *57* (3), 1505-1509.

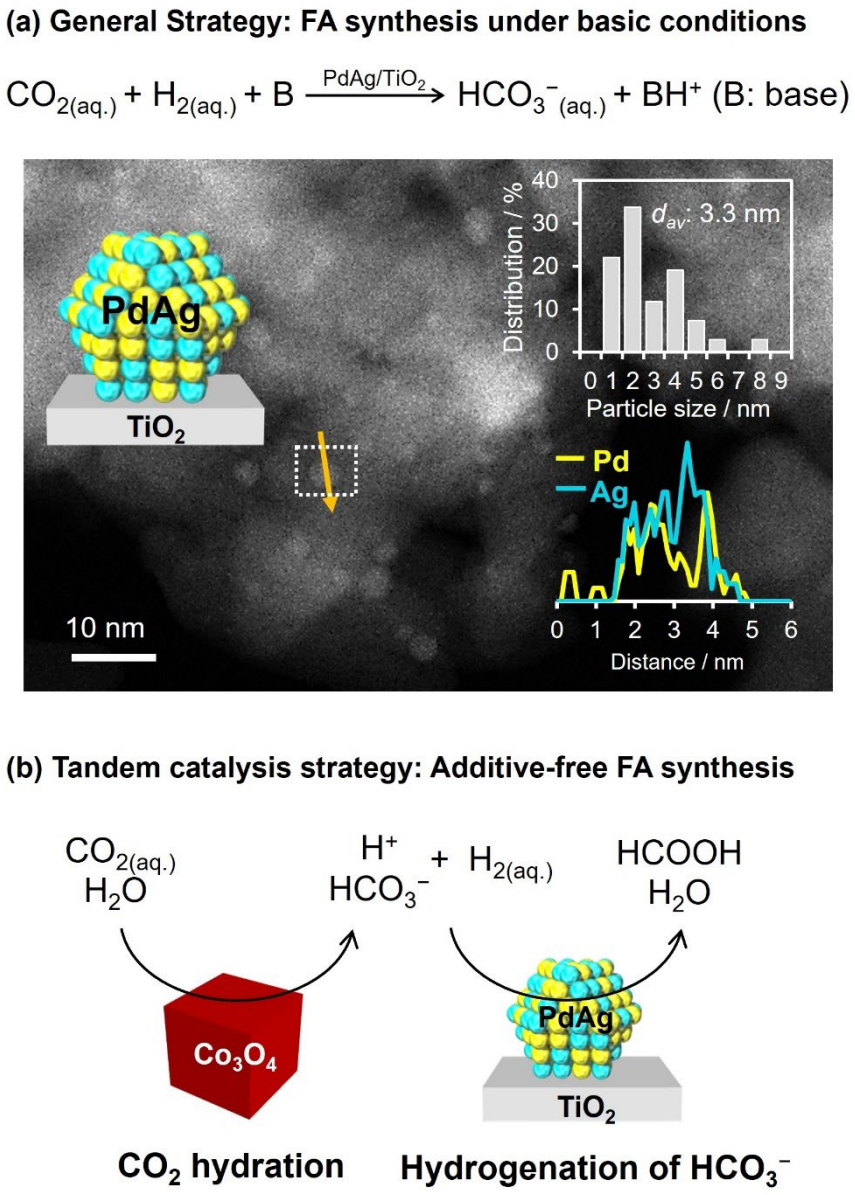

Figure 1 (a) Reaction scheme for general strategy for FA synthesis by PdAg/TiO_2 under basic conditions, HAADF-STEM image, particle size distribution for PdAg, and elemental distributions as determined by cross-sectional EDX line profiling. (b) Schematic illustration of heterogeneous tandem catalysis strategy for additive-free CO_2 hydrogenation into FA in water using Co_3O_4 cocatalyst in conjunction with PdAg/TiO_2 hydrogenation catalyst.

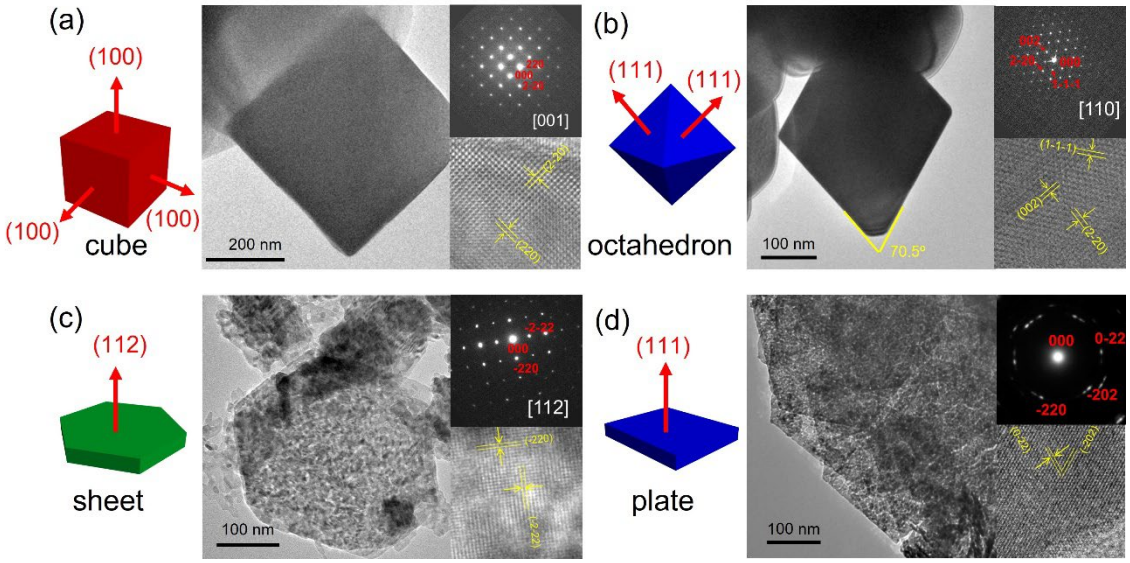

Figure 2. TEM image, SAED pattern, and high-resolution TEM image of (a) Co_3O_4 cube, (b) Co_3O_4 octahedron, (c) Co_3O_4 sheet, and (d) Co_3O_4 plate.

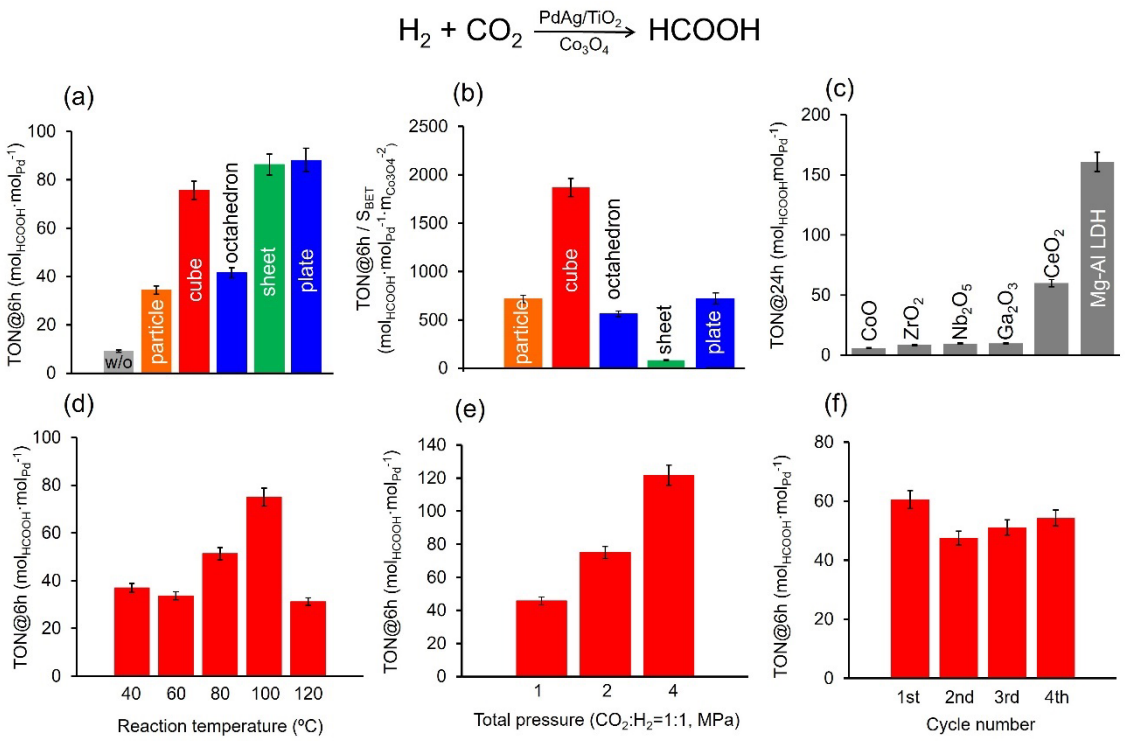

Figure 3. Comparison of catalytic activity under additive-free conditions: (a) effect of addition of Co_3O_4 cocatalyst; (b) TON based on surface area of Co_3O_4 cocatalyst (TON/S_{BET}); (c) catalytic results obtained using other metal oxides and hydroxides as cocatalyst; (d) effect of reaction temperature using Co_3O_4 cocatalyst; (e) effect of total pressure using Co_3O_4 cocatalyst; and (f) recycling experiment using Co_3O_4 cocatalyst.

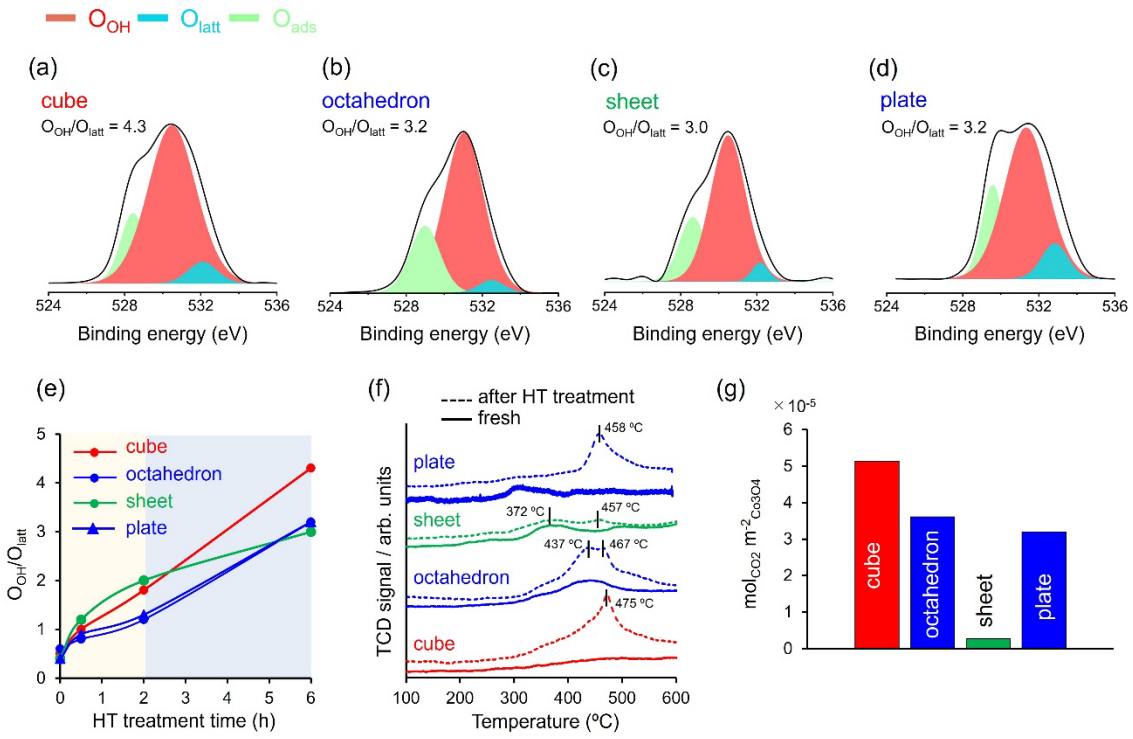

Figure 4. O 1s XPS spectra after hydrothermal (HT) treatment at 100 °C for 6 h of (a) Co_3O_4 cubes, (b) Co_3O_4 octahedra, (c) Co_3O_4 sheets, and (d) Co_3O_4 plates. (e) O_{OH}/O_{latt} ratio as function of HT treatment time. (f) CO_2-TPD profiles before and after hydrothermal (HT) treatment at 100 °C for 6 h of series of Co_3O_4. (g) Comparison of total amount of adsorbed CO_2 based on surface area ($mol_{CO2} \cdot m^{-2}{}_{Co3O4}$).

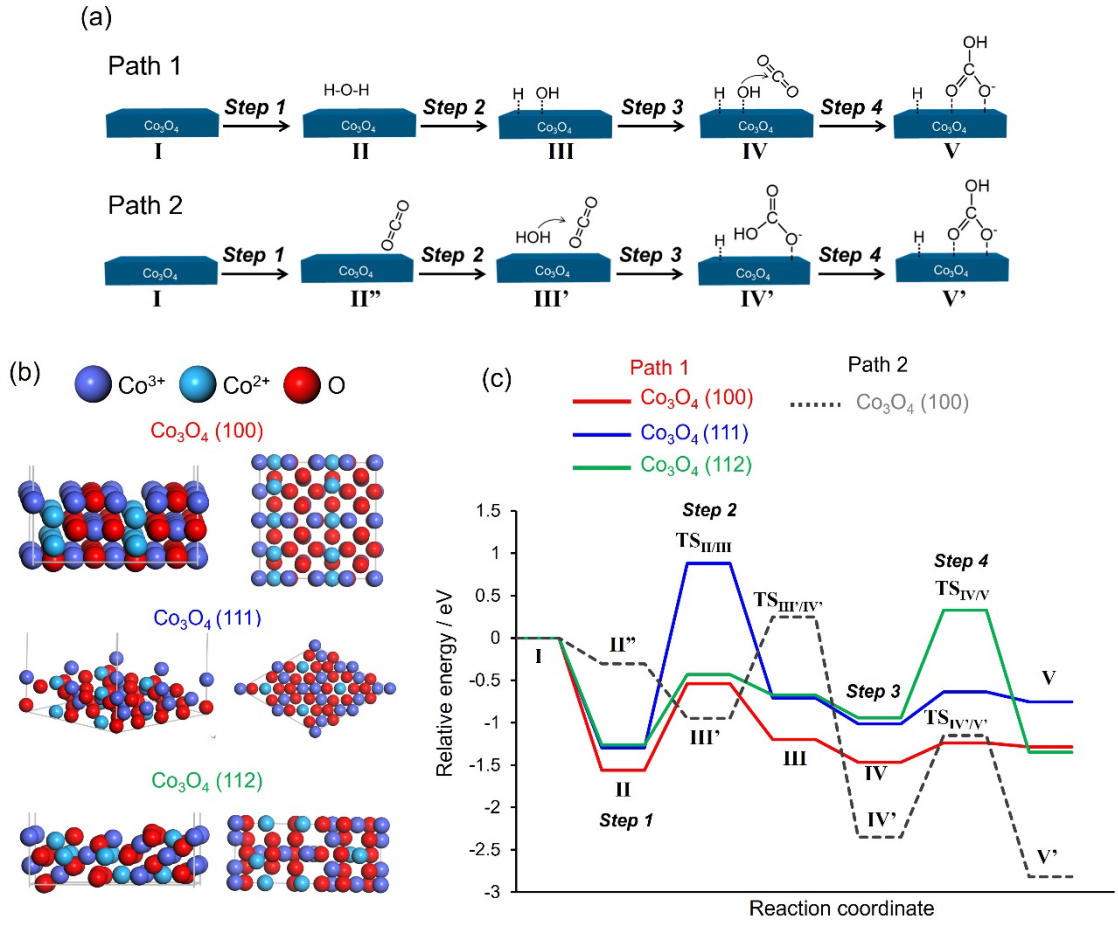

Figure 5. (a) Possible catalytic cycle for CO_2 hydration over Co_3O_4. (b) Co_3O_4(100), Co_3O_4(111), and Co_3O_4(112) slab models for cube, octahedron/plate, and sheet, respectively, in DFT calculations of activation energy. (c) Potential energy profiles for CO_2 hydration. Transition states were determined using the nudged elastic band method, and the activation energy was defined as the energy difference between the TS and reactant.

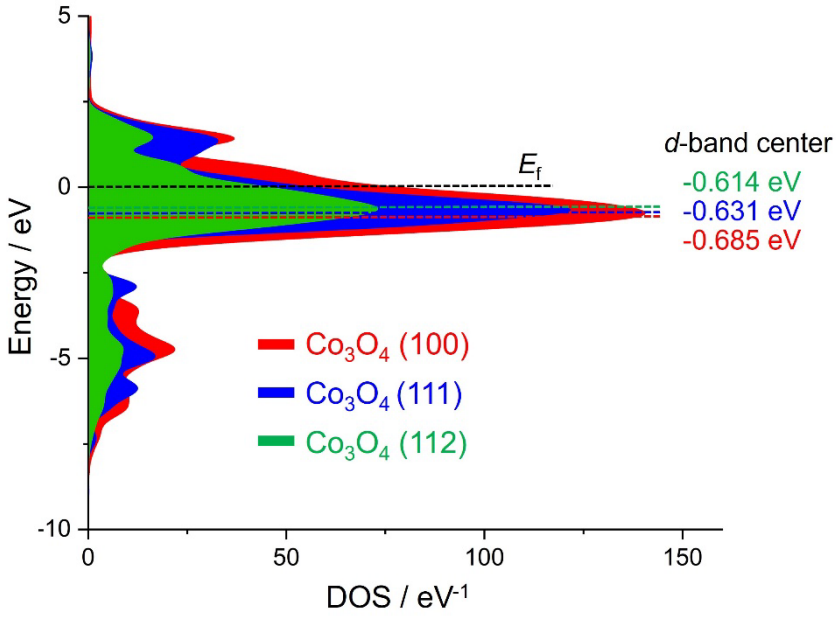

Figure 6. Calculated DOS plots and the d-band center for Co_3O_4(100), Co_3O_4(111), and Co_3O_4(112) slab models.

TOC Graphics